



Perovskite $\text{La}_x\text{M}_{1-x}\text{Ni}_{0.8}\text{Fe}_{0.2}\text{O}_3$ catalyst for steam reforming of toluene: Crucial role of alkaline earth metal at low steam condition

U. Oemar, M.L. Ang, W.F. Hee, K. Hidajat, S. Kawi*

Department of Chemical and Biomolecular Engineering, National University of Singapore, 4 Engineering Drive 4, Singapore 117576, Singapore

ARTICLE INFO

Article history:

Received 5 April 2013

Received in revised form

19 September 2013

Accepted 1 October 2013

Available online 10 October 2013

Keywords:

Alkaline earth metal

Steam effect

Toluene reforming

Nickel–iron alloy

Hydrogen production

ABSTRACT

The effect of alkaline earth metal (Mg, Ca, and Sr) substitution to $\text{LaNi}_{0.8}\text{Fe}_{0.2}\text{O}_3$ perovskite catalyst was investigated for steam reforming of toluene as a model compound of tar at various steam amounts. Catalytic performance of $\text{La}_{0.8}\text{Sr}_{0.2}\text{Ni}_{0.8}\text{Fe}_{0.2}\text{O}_3$ (LSNFO) catalyst at high steam condition ($\text{S/C} = 3.4$) is higher than the activity of $\text{La}_{0.8}\text{Mg}_{0.2}\text{Ni}_{0.8}\text{Fe}_{0.2}\text{O}_3$ (LMNFO) and $\text{La}_{0.8}\text{Ca}_{0.2}\text{Ni}_{0.8}\text{Fe}_{0.2}\text{O}_3$ (LCNFO) catalysts due to higher amount of active sites and higher amount of lattice oxygen on LSNFO catalyst. However, the activity of LSNFO catalyst is still lower than the activity of $\text{LaNi}_{0.8}\text{Fe}_{0.2}\text{O}_3$ (LNFO) catalyst even though carbon deposition on spent LSNFO catalyst is the lowest among other catalysts. Interestingly, the activity of LSNFO catalyst is comparable with the activity of LNFO catalyst at S/C of 2 and outperforms LNFO catalyst at S/C of 1. Moreover, the carbon deposition on LNFO catalyst increases with increasing temperature while it decreases with increasing temperature on LSNFO catalyst due to lattice oxygen desorbed at 700–800 °C. Further characterization shows that water is adsorbed strongly on LSNFO catalyst and is only able to desorb at higher temperature near the reaction temperature. This strongly adsorbed water property of LSNFO catalyst enables this catalyst to have better catalytic performance at low steam condition.

© 2013 Elsevier B.V. All rights reserved.

1. Introduction

Utilization of biomass as a renewable energy source has been receiving a great interest due to its abundance, lower sulfur content, and CO_2 -neutral emissions compared to fossil fuels [1]. The biomass can be converted to syngas which can be used for generating electricity and for chemical synthesis via Fischer–Tropsch to produce methanol, dimethylether, and other chemical products [1–4]. However, the main problem of biomass is formation of tar (complex mixture of aromatic heavy hydrocarbons with toluene as the major component, followed by naphthalene) which can cause a wide range of problems in downstream process units since the condensation and deposition of tar result in plugging and fouling of turbines, pipelines and engines. Non-catalytic process for decreasing the tar amount by cracking tar to small gases molecules always requires high temperature, which is unfavorable in terms of energy efficiency. Therefore, catalyst is required to lower down the reaction temperature. Moreover, the catalyst can also improve the quality of product gas in terms of composition of carbon monoxide to hydrogen ratio for downstream process [5].

Non-noble metal catalysts such as Ni, Co, and Fe have been studied for steam reforming of tar as well as toluene as the model compound of tar. Nickel catalyst is one of the common catalysts

for steam reforming of toluene due to its low cost, wide availability, and high activity [6–10]. However, nickel catalyst is prone to carbon deposition, causing catalyst deactivation in short time. In order to improve the activity and stability of Ni catalyst, addition of second metal as a promoter is recommended. Our previous study [11] showed that addition of Fe to Ni catalyst in perovskite type oxide enhanced the catalytic activity and stability in steam reforming of toluene due to synergistic interactions of Ni and Fe to form bimetallic Ni–Fe particles. The similar conclusion was obtained by Tomishige et al. [12,13] for Ni–Fe/ Al_2O_3 catalyst in cellulose gasification.

Cobalt catalyst was also studied for steam reforming of toluene due to its low cost. The catalytic performance of Co catalysts has been reported to be comparable to that of Ni catalysts [14–16]. Similar to Ni–Fe catalysts, the bimetallic Co–Fe catalyst was also reported to have higher activity than the monometallic Co catalyst [17,18].

To further improve the catalyst performance, modification of catalyst support is suggested in literature. Catalysts with basic properties tend to decrease the rate of coke formation, in many reforming reactions, such as steam reforming of biomass tar [19–23], CO_2 reforming of methane [24,25], steam reforming of methane [26], steam reforming of ethanol [27–29], and which in turn leads to reduced catalyst deactivation over time and helps to increase the stability of the catalyst. The addition of basic metal oxides (Na_2O , K_2O , MgO , and CaO) to the Ni catalyst in CO_2 reforming of methane enhanced CO_2 adsorption, resulting

* Corresponding author. Tel.: +65 6516 6312; fax: +65 6779 1936.

E-mail address: chekawis@nus.edu.sg (S. Kawi).

in more adsorbed oxygen atoms (O_{ad}) [25]. The higher amount of adsorbed oxygen atoms (O_{ad}) prevented adsorbed hydrogen-deficient hydrocarbon species ($CH_{x,ad}$) to decompose to surface carbon since the adsorbed oxygen species could easily react with the adsorbed hydrogen-deficient hydrocarbon species ($CH_{x,ad}$) to form CO. In steam reforming of ethanol, the addition of basic metal oxide such as CaO to Ni catalyst could prevent the formation of the more stable crystalline carbon which is difficult to be removed, thus resulting in higher catalyst stability. Moreover, it was reported that Ca addition promoted water adsorption and provided abundance of adsorbed OH groups in Ni catalyst which could facilitate the C–C break, resulting in higher ethanol conversion [27–29]. In biomass gasification, it was also reported that the basicity was a favorable character for tar decomposition catalysts since the higher basicity of catalyst enhanced the catalyst activity [30].

Addition of oxygen gas to the steam reforming of toluene reaction has been reported to enhance the cracking of tar [31,32]. However, since purified oxygen is expensive while the use of air in steam reforming of toluene could result in lower heating value of the product gas because of dilution of the gas by nitrogen, it was proposed to use the catalyst containing oxygen storage/vacancy to increase the catalyst activity and stability [33–35]. Zhang et al. [36] reported that the addition of CeO_2 to Ni/Al_2O_3 catalyst could inhibit carbon deposition and coking. The similar conclusion was reported by Brown et al. [37] for addition of CeO_2 to $Ni/olivine$ catalyst. Furthermore, Rirksomboon et al. [38] reported that the incorporation of manganese ions to ceria lattice on Ni/CeO_2-ZrO_2 catalyst could improve the oxygen storage capacity and the oxygen mobility on the catalyst surface, resulting in faster carbon removal. Atong et al. [39] substituted Ce into $LaNiO_3$ perovskite type oxide and reported that the reducibility of $La_{0.6}Ce_{0.4}NiO_3$ perovskite catalyst was improved by introduction of Ce. As a result, the catalyst had the highest activity at 800 °C and stability for 3 h of reaction time.

From above literatures, it clearly shows that development of catalyst for steam reforming of toluene should consider addition of basic metal oxide and oxygen vacancy simultaneously to enhance the catalyst activity and stability. In order to accommodate these two requirements, our approach in this study is by using perovskite-type oxide. Perovskite catalyst is a well-defined mixed oxide catalyst with general chemical formula of ABO_3 , whereby A-site is lanthanide metal (La, Ba, Ca, and Sr) and B-site is transitional metal (Ni, Co, Fe, and Cu). After full reduction, the structure will collapse and form metal on catalyst support. By partially substituting the A-site with alkaline earth metal oxide, the perovskite catalyst can have more basic sites. Moreover, the partial substitution can cause the structural defects, resulting in oxygen nonstoichiometry [40], i.e. lattice oxygen. Our previous results showed that $LaNi_{0.8}Fe_{0.2}O_3$ catalyst had comparable activity but higher stability than $LaNiO_3$ catalyst. By partial substitution with alkaline metal oxide such as Ca, Mg, or Sr to $LaNi_{0.8}Fe_{0.2}O_3$ catalyst, it is expected that the catalyst would have much higher activity and stability. The catalytic performance of the catalysts in terms of activity and stability is studied for steam reforming of toluene. Various characterizations of fresh, reduced, and spent catalysts are also performed to elucidate the effect of alkaline earth metal addition to Ni catalyst in catalyst performance.

2. Experimental

2.1. Catalyst synthesis

A series of Ni–Fe perovskite catalysts was synthesized using sol gel method using citric acid as the complexing agent. The reagents used were $Ni(NO_3)_2 \cdot 6H_2O$ (Merck), $Fe(NO_3)_3 \cdot 9H_2O$ (Aldrich),

citric acid monohydrate (Sigma–Aldrich), $La(NO_3)_3 \cdot 6H_2O$ (Strem), $Sr(NO_3)_2$ (Sigma–Aldrich), $Mg(NO_3)_2 \cdot 6H_2O$ (Sigma–Aldrich), and $Ca(NO_3)_2 \cdot 4H_2O$ (Sigma–Aldrich). Firstly, the required amounts of $Ni(NO_3)_2 \cdot 6H_2O$, $Fe(NO_3)_3 \cdot 9H_2O$, citric acid monohydrate, $La(NO_3)_3 \cdot 6H_2O$ and $Sr(NO_3)_2$ or $Mg(NO_3)_2 \cdot 6H_2O$ or $Ca(NO_3)_2 \cdot 4H_2O$ were dissolved in deionized water. The molar ratio of Ni/Fe of the best performance produced from the $LaNi_xFe_{1-x}O_3$ catalyst was 8:2 based on our previous study [11], while the molar of the active metals to the mixed lanthanum–alkali earth metals was 1:1 and the molar ratio of the mixed lanthanum–alkali earth metals to that of citric acid monohydrate added was 1:2. The solution obtained was continuously stirred at 55 °C until a gel-like structure was formed. The catalysts were then dried in an oven at 100 °C overnight and calcined under air at 400 °C for 30 min, followed by calcination at 850 °C for 7 h. Finally, the catalysts were crushed and sieved to obtain particle sizes that are smaller than 125 μm .

2.2. Characterization methods

2.2.1. X-ray diffraction

The X-ray diffraction pattern of each catalyst was measured on a Shimadzu XRD-6000 diffractometer using Cu $K\alpha$ radiation. The catalyst was placed on an aluminum slide and scanned from 2θ of 20° to 80° with a ramp rate of 2°/min. The beam voltage and current used were 40 kV and 30 mA, respectively.

2.2.2. TPR, TPD, TPSR, and pulse titration measurement

Temperature-programmed reduction- H_2 (TPR) measurement for fresh catalyst was performed on Quantachrome ChemBET-3000. Prior to TPR measurement, 0.05 g of catalyst was outgassed in He for 1 h at 300 °C to remove any impurities and then cooled down to room temperature. 5% H_2/N_2 gas was then introduced to the catalyst while temperature of furnace was increased at a heating rate of 10 °C/min to 1000 °C.

Temperature-programmed desorption of oxygen (TPD- O_2) for reduced catalyst was also performed on Quantachrome ChemBET-3000. 0.1 g of sample was initially reduced under H_2 for 1 h at 600 °C, followed by cooling down to room temperature prior to the TPD- O_2 measurement. Purified He gas was then introduced to the system to purge out all the remaining oxygen. The TPD- O_2 measurement was started from room temperature to maximum furnace temperature of 1100 °C under a heating rate of 10 °C/min.

Temperature-programmed desorption of water (TPD- H_2O) for reduced catalyst was performed on the fixed-bed reactor system coupled with Thermostar Mass Spectrometer GSD 300 T. Prior to TPD- H_2O measurement, 0.05 g of sample was reduced under H_2 for 1 h at 600 °C, followed by cooling down under He to room temperature. The water was then introduced to the sample at room temperature for 30 min, followed by purging under purified He gas at 100 °C for 1 h. The TPD- H_2O measurement was started from 100 °C to maximum temperature of 600 °C under a heating rate of 10 °C/min.

Temperature-programmed surface reaction of water (TPSR- H_2O) was also performed on the fixed-bed reactor system coupled with Thermostar Mass Spectrometer GSD 300 T. 0.1 g of sample was pre-treated at the same condition with TPD- H_2O . The water was then introduced to the sample after cooling down to room temperature using He as a carrier gas at room temperature for 30 min, followed by ramping the furnace temperature to 800 °C under a heating rate of 10 °C/min.

In order to calculate the amount of active sites and metal dispersion, pulse titration was performed on the Quantachrome ChemBET-3000 according to the method reported in recent literature [41]. The H_2 -TPR was initially performed using 0.1 g of sample up to 600 °C, followed by cooling down to room temperature. Purified N_2O gas was then introduced to the system by pulse injection

until saturation. The H_2 -TPR was repeated up to 600 °C. The amount of active sites can be calculated from the amount of adsorbed N_2O while the dispersion can be calculated by comparing the second TPR to the first TPR results.

2.2.3. X-ray photoelectron spectroscopy

The X-ray photoelectron spectroscopy was performed on Kratos AXIS Ultra DLD using concentric hemispherical analyzer and Al $K\alpha$ gun as the X-ray source. Prior to the analysis, the catalyst was reduced at 600 °C under H_2 for 1 h which is the same as the reduction condition during reaction. The sample was then mounted on the standard sample stub using double-sided adhesive tapes. All binding energies were referenced to C 1s hydrocarbon peak at 284.5 eV.

2.2.4. TEM

The metal particle size was measured visually using HRTEM system JEOL JEM-2100F. The average metal size was then calculated over 100 particles. Prior to the observation, the catalyst was reduced at 600 °C under H_2 for 1 h. The sample was then ultrasonically dispersed in ethanol and spread over perforated copper grids.

2.3. Catalytic reaction

The catalytic reaction was carried out in a fixed bed quartz reactor with an inner diameter of 4 mm and a length of 400 mm. 0.03 g of catalyst was used in each test and held by quartz wool placed in the middle of the reactor. Prior to the catalytic reaction, the catalyst was reduced in 30 mL/min H_2 at 600 °C for 1 h, followed by purging in 120 mL/min helium while the temperature was increased to the reaction temperature. The water and toluene were vaporized at 300 °C in a preheater and mixed with 120 mL/min of He before entering the main reactor in the vapor state. The reaction products were then passed through a cold trap at temperature of 5 °C to condense any moisture formed. The non-condensable gas product was analyzed using a gas chromatograph (HP 6890) equipped with a Carboxen column and a TCD detector. The chromatogram showed peak areas for all reacted gases which were then converted to volume-% through a calibration curve. The total flow rate of the product gases was measured using bubble flow meter. The conversion of toluene was expressed in term of carbon conversion and calculated using the following formula:

$$X_{\text{Toluene}}(\%) = \frac{n_{\text{CO}} + n_{\text{CO}_2}}{7 * n_{\text{T,in}}} \times 100$$

where n is molar flow rate of each gas.

The total amount of deposited carbon on the spent catalysts was measured using thermogravimetric analysis (TGA) on a Shimadzu DTG-60 thermogravimetric analyzer. Around 10 mg of spent catalyst was used in each TGA experiment and heated in air to 800 °C with a heating rate of 10 °C/min.

3. Results and discussion

3.1. XRD – structural analysis

Figure S1 (see supplementary information) shows the XRD patterns of fresh $\text{La}_x\text{Sr}_{1-x}\text{Ni}_{0.8}\text{Fe}_{0.2}\text{O}_3$ catalyst. The $\text{LaNi}_{0.8}\text{Fe}_{0.2}\text{O}_3$ catalyst shows the diffraction patterns of pure perovskite structure (PDF-88-0633). With the substitution of Sr, only $\text{La}_{0.8}\text{Sr}_{0.2}\text{Ni}_{0.8}\text{Fe}_{0.2}\text{O}_3$ catalyst shows matching diffraction patterns with $\text{LaNi}_{0.8}\text{Fe}_{0.2}\text{O}_3$ catalyst. This proves that only a small amount of Sr could make a perfect incorporation of Sr^{2+} to La^{3+} site of $\text{La}_x\text{Sr}_{1-x}\text{Ni}_{0.8}\text{Fe}_{0.2}\text{O}_3$ catalyst. Few additional peaks can be observed for catalyst with substitution of Sr more than 0.2, which are

attributed to the presence of SrO oxide phase. The presence of this SrO oxide phase shows the segregation of Sr^{2+} on the surface to form SrO oxide phase due to the fact that the ionic radius of Sr^{2+} ion (11.8 Å) is larger than the ionic radius of La^{3+} (10.3 Å). This XRD result clearly shows that the perfect incorporation of Sr^{2+} to $\text{LaNi}_{0.8}\text{Fe}_{0.2}\text{O}_3$ catalyst can be only achieved at Sr maximum of 0.2. Based on the above result, the amount of alkaline earth metal added to $\text{LaNi}_{0.8}\text{Fe}_{0.2}\text{O}_3$ catalyst was fixed at 0.2.

Figure S2 (see supplementary information) shows the XRD result of fresh $\text{La}_{0.8}\text{M}_{0.2}\text{Ni}_{0.8}\text{Fe}_{0.2}\text{O}_3$ catalysts ($M = \text{Ca}, \text{Mg}, \text{and Sr}$). It can be seen that all catalysts show identical patterns of pure perovskite structure. However, the intensity of the strongest peak at 2θ of 32.7° decreases from $\text{La}_{0.8}\text{Ca}_{0.2}\text{Ni}_{0.8}\text{Fe}_{0.2}\text{O}_3$ (named as LCNFO), $\text{La}_{0.8}\text{Sr}_{0.2}\text{Ni}_{0.8}\text{Fe}_{0.2}\text{O}_3$ (named as LSNFO) to $\text{La}_{0.8}\text{Mg}_{0.2}\text{Ni}_{0.8}\text{Fe}_{0.2}\text{O}_3$ (named as LMNFO). This result shows that LCNFO has the biggest crystal size while LMNFO has the smallest crystal size.

Fig. 1a shows the XRD patterns of reduced $\text{La}_{0.8}\text{M}_{0.2}\text{Ni}_{0.8}\text{Fe}_{0.2}\text{O}_3$ ($M = \text{Ca}, \text{Mg}, \text{and Sr}$) catalysts. It can be seen that the diffraction peaks on those catalysts are totally different from the ones on fresh catalysts, showing that the perovskite structure in those catalysts has been destroyed to form metal on catalyst support, which is in agreement with the report in literature [42]. The peak intensity of all catalysts is also similar showing that the crystallinity among all catalysts are the same. This result is also supported by the BET result (Table 1) of reduced catalysts showing similar surface area at around 6–10 m²/g.

In order to show the presence of metal on the reduced $\text{La}_{0.8}\text{M}_{0.2}\text{Ni}_{0.8}\text{Fe}_{0.2}\text{O}_3$ ($M = \text{Ca}, \text{Mg}, \text{and Sr}$) catalysts, narrow scan was performed and the result is shown in Fig. 1b. It can be seen that the diffraction peak at around 44.4°, corresponding to the Ni-rich Ni–Fe bimetallic particles [12], is observed to be very small on LMNFO catalyst while LCNFO catalyst shows sharper peak than LSNFO catalyst. To quantify the crystal size of metallic particles, Scherrer equation was used on the diffraction peak on those catalysts and the results are 11.8 nm, 16.3 nm, and 14.1 nm for LMNFO, LCNFO, and LSNFO catalysts respectively. For comparison, the crystal size of LNFO catalyst is 13.9 nm. Compared to the BET surface area of reduced catalysts, it is observed that the BET surface area is to be lower at bigger crystal size of Ni–Fe particles. However, the calculation of crystal size obtained from XRD results is only a rough estimation and not as accurate as TEM results (Section 3.6) because the peak width on the bimetallic particles is due to not only the average particle size but also the uniformity in the composition of each particle.

It is well known that the crystal lattice parameter of a solid solution alloy is a linear combination of the lattice constant of each components, according to Vegard's law [17]. Assuming the homogeneous composition of each phase, the average Fe/Ni ratio of bcc Ni–Fe alloy on the reduced catalysts can be calculated using the $d(200)$ spacings of fcc Ni metal and fcc γ -Fe metal. The average Fe/Ni ratios are 0.25, 0.32, 0.22, 0.27, for LNFO, LMNFO, LCNFO, and LSNFO, respectively. All reduced catalysts except LMNFO catalyst show the average Fe/Ni ratio of 0.25 which is the same with the Fe/Ni ratio in the perovskite structure.

3.2. H_2 TPR – reducibility analysis

Fig. 2 shows the TPR profile of $\text{La}_{0.8}\text{M}_{0.2}\text{Ni}_{0.8}\text{Fe}_{0.2}\text{O}_3$ catalyst ($M = \text{Ca}, \text{Mg}, \text{Sr}$) compared to TPR profile of $\text{LaNi}_{0.8}\text{Fe}_{0.2}\text{O}_3$ catalyst. For $\text{LaNi}_{0.8}\text{Fe}_{0.2}\text{O}_3$ catalyst, two peaks at low temperature and one peak at high temperature are observed. The peaks at low temperature can be attributed to the reduction of Ni^{3+} to Ni^{2+} , which is in agreement with our previous study and literature [11,43]. Meanwhile, the peak at high temperature can be attributed to the reduction of strongly interacting Fe with catalyst support with the aid of Ni [44]. The presence of this peak indicates the interaction

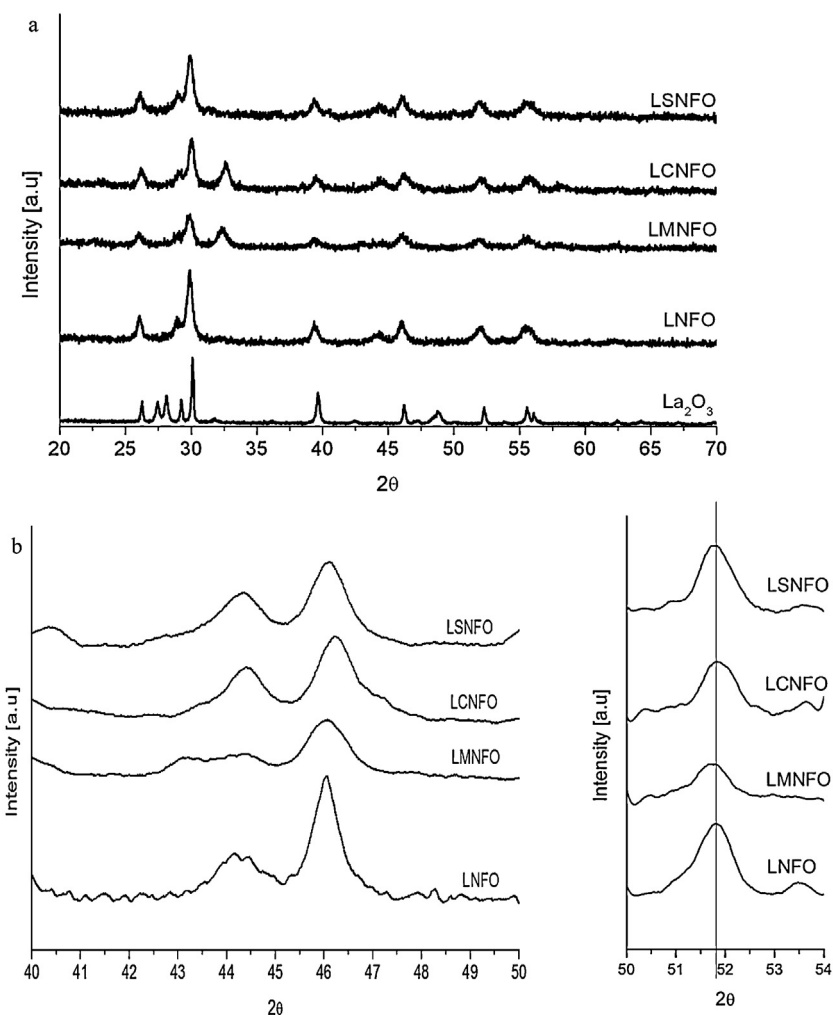


Fig. 1. (a) Wide scan and (b) narrow scan of XRD patterns of reduced $\text{La}_{0.8}\text{M}_{0.2}\text{Ni}_{0.8}\text{Fe}_{0.2}\text{O}_3$ catalysts.

between Ni and Fe to form bimetallic particles which is also in agreement with the XRD result. Literature studies have concluded that for catalysts that contain Ni, Fe and La, a fraction of the Fe undergoes reduction with the aid of Ni and Ni–Fe bimetallic particles are formed after the reduction process [44–49].

With the substitution of alkaline earth metal, the TPR profile of the $\text{La}_{0.8}\text{M}_{0.2}\text{Ni}_{0.8}\text{Fe}_{0.2}\text{O}_3$ catalyst is significantly changed. For LSNFO catalyst, there is an additional peak at around 485 °C which

can be attributed to the reduction of NiO since it was reported that the presence of Sr can interrupt the Ni– La_2O_3 interaction [41]. In addition, the peak at high temperature is observed to be broader than the one on LNFO catalyst. The presence of broader peak could be due to interaction of metal and the support as well as the reduction of lattice oxygen which is later discussed from TPD– O_2 results. LCNFO catalyst shows similar phenomenon where the peak at lower temperature region around 200–525 °C could be attributed

Table 1
Physicochemical properties of the prepared catalysts.

Catalyst	BET surface area (m^2/g)		Content (mmol/g)		H_2 consumption ^a (mmol/g)	Fe/Ni atomic ratio in particles ^b	Ni-based reduction degree ^c (%)	Reduced Fe amount ^d (mmol/g)	Metal particle size ^e (nm)	N_2O adsorption ^f (mmol/g)	Dispersion ^g (%)
	Fresh	Reduced	Ni	Fe							
LNFO	4.29	6.91	3.26	0.82	3.52	0.25	107.8	0.17	12.3	0.44	12.5
LMNFO	2.63	10.49	3.26	0.82	2.29	0.32	71.6	–	7.4	0.45	19.6
LCNFO	2.97	6.36	3.26	0.82	3.41	0.25	104.6	0.15	12.9	0.39	11.43
LSNFO	2.78	7.72	3.26	0.82	3.58	0.27	111.9	0.21	9.1	0.59	16.5

^a H_2 consumption below 600 °C in TPR profiles shown in Fig. 2.

^b Calculated from $d(200)$ spacing of XRD result by the Vegard's law: $d_{\text{Ni-Fe}} = d_{\text{Ni}} \times \text{Ni}/(\text{Ni} + \text{Fe}) + d_{\text{Fe}} \times \text{Fe}/(\text{Ni} + \text{Fe})$, where d_{Ni} and d_{Fe} are 0.1762 nm (JCPDS 01-070-1849) and 0.1823 nm (JCPDS 01-089-4185), respectively.

^c Stoichiometry of the Ni reduction is $\text{Ni}^{2+} + \text{H}_2 \rightarrow \text{Ni}^0 + 2\text{H}^+$.

^d H_2 consumption > Ni content is assigned to the reduction of Fe. Stoichiometry of Fe reduction is $2\text{Fe}^{3+} + 3\text{H}_2 \rightarrow 2\text{Fe}^0 + 6\text{H}^+$.

^e Average metal particle size measured from 100 particles observed in TEM results.

^f Measured by N_2O pulse titration at room temperature.

^g Calculated by comparing TPR– H_2 before and after N_2O pulse titration up to 600 °C.

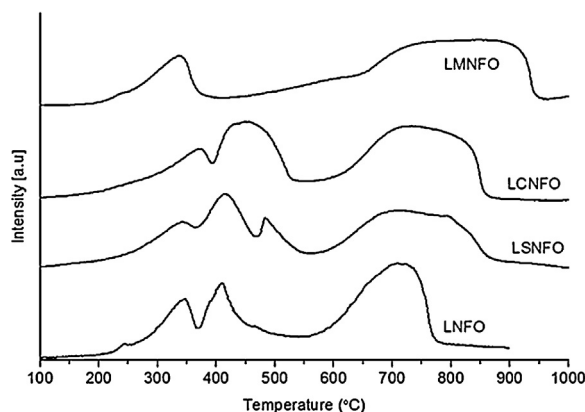


Fig. 2. TPR profiles of $\text{La}_{0.8}\text{Mg}_{0.2}\text{Ni}_{0.8}\text{Fe}_{0.2}\text{O}_3$ catalysts.

to the reduction of Ni^{3+} to Ni^{2+} while the peak at high temperature could be assigned to the reduction of metal strongly interacting with the support as well as the reduction of the lattice oxygen. However, for LMNFO catalyst, the peak at low temperature is much smaller than the one on LNFO catalyst, implying the difficulty of LMNFO catalyst to be reduced at lower temperature. Moreover, the peak at high temperature is also observed to be much broader than the peak on the LSNFO and LCNFO catalysts. Since LMNFO catalyst does not show any desorption peak of oxygen in TPD- O_2 (as shall be shown in Section 3.3), this peak must be attributed to the stronger interaction of the metal (Ni and Fe) and the support with the substitution of Mg. It has been reported in literature that Ni can form solid solution with Mg which results in very fine particles [50,51].

Table 1 shows the amount of H_2 consumption calculated up to 600 °C which is the reduction temperature in this study. It can be seen that the amount of H_2 consumption decreases in the order of $\text{LSNFO} > \text{LNFO} > \text{LCNFO} > \text{LMNFO}$. By comparing the H_2 consumption with the amount of Ni and Fe in the catalysts, it can be seen that the Ni reduction degree is more than 100% for LNFO, LCNFO, and LSNFO catalysts, while it is less than 100% for LMNFO catalyst with the assumption that H_2 consumption is used to reduce all Ni with the ratio H_2/Ni of 1/1. The H_2 consumption beyond 100% Ni reduction degree can be attributed to the reduction of Fe. Hence, some Fe is reduced for LNFO, LCNFO, and LSNFO catalyst, while no Fe is reduced for LMNFO catalyst. This result indicates that the LMNFO catalyst will have the lowest activity compared to other catalysts which will be later shown in the reaction results in Section 3.7.

It is important to point out that all catalysts are partially reduced at 600 °C. Hence, the reduced state of the catalyst is a part of incorporated Ni–Fe deposited on the perovskite oxide, which can be written as $\text{Ni-Fe/LaNi}_x\text{Fe}_y\text{O}_{3-\delta}$, $\text{Ni-Fe/La}_{0.8}\text{Mg}_{0.2}\text{Ni}_x\text{Fe}_y\text{O}_{3-\delta}$, $\text{Ni-Fe/La}_{0.8}\text{Ca}_{0.2}\text{Ni}_x\text{Fe}_y\text{O}_{3-\delta}$, $\text{Ni-Fe/La}_{0.8}\text{Sr}_{0.2}\text{Ni}_x\text{Fe}_y\text{O}_{3-\delta}$ for reduced LNFO, LMNFO, LCNFO, and LSNFO catalysts, respectively. In this case, the active site of the steam reforming of toluene reaction is the reduced Ni–Fe instead of the incorporated Ni–Fe on the perovskite surface.

3.3. TPD O_2

Since perovskite catalyst is well known to have lattice oxygen mobility, TPD- O_2 was performed on reduced catalyst to see the desorption temperature of the lattice oxygen. Fig. 3 shows the TPD O_2 of reduced LNFO, LSNFO, LCNFO, and LMNFO catalysts. It can be seen that LNFO catalyst shows the trend of increasing intensity starting from 1000 °C while LMNFO catalyst does not show any peak. On the other hand, LSNFO catalyst shows a peak at around 700–800 °C while LCNFO catalyst shows only increasing intensity without obvious peak. This result shows that the lattice oxygen in

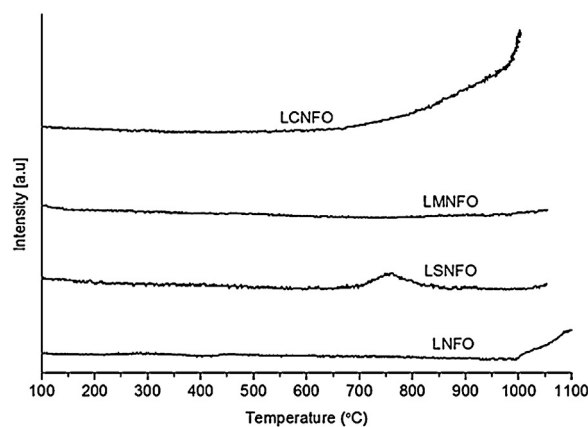


Fig. 3. TPD- O_2 profiles of $\text{La}_{0.8}\text{Mg}_{0.2}\text{Ni}_{0.8}\text{Fe}_{0.2}\text{O}_3$ reduced catalysts.

LSNFO catalyst is more mobile than lattice oxygen in other catalysts. In addition, this result also indicates that LSNFO catalyst may show good stability for steam reforming of toluene at reaction temperature of 700–800 °C since only at that temperature, the lattice oxygen can help to remove carbon deposition.

It is well known from literature that the oxygen can be desorbed at lower and higher temperature [52]. The oxygen desorption peak at lower temperature (at around 400 °C) can be assigned as chemisorbed oxygen species on the surface, commonly named as α -oxygen species [53–55]. On the other hand, the oxygen peak observed at temperatures around 700–800 °C can be attributed to the lattice oxygen species (β -oxygen species) released from the bulk structure of the catalyst [53–55]. It has also been reported that the α -oxygen species is more active than β -oxygen species at 300 °C [56]. However, since steam reforming of toluene reaction is normally performed at around 600–800 °C, the lattice oxygen (β -oxygen) species may play an important role in steam reforming of toluene reaction.

3.4. XPS of reduced catalysts

In order to confirm the amount and the mobility of lattice oxygen of the reduced catalysts, the XPS O1s is therefore performed for all reduced catalysts and the result is shown in Fig. 4. The XPS spectra show similar identical peaks for all catalysts. The first peak at around 528.0–529.0 eV can be attributed to the oxygen ions in the crystal lattice (O^{2-}) [41,57–59], whereas the second peak at around 530.6 eV corresponds to the adsorbed oxygen species, and the third peak at around 532.0 eV corresponds to the adsorbed water. However, the position of the peak, especially the first peak

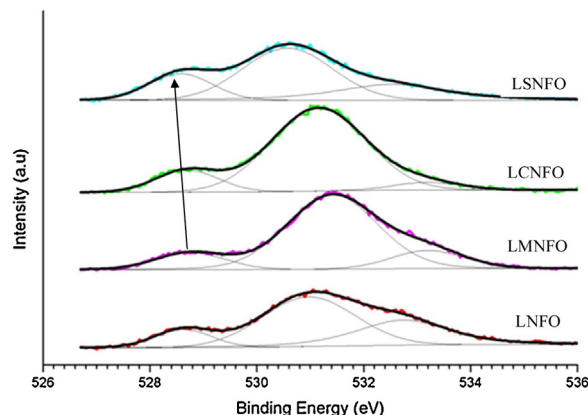


Fig. 4. XPS O 1s of reduced catalysts.

Table 2
Amount of each surface oxygen species.

Catalyst	Surface oxygen species*						
	Lattice oxygen			Adsorbed oxygen		Adsorbed water	
	B.E (eV)	% area	%area/S.A. ^a	B.E (eV)	% area	B.E (eV)	% area
LSNFO	528.58	19.25	2.49	530.57	53.80	532.51	26.95
LCNFO	528.69	14.20	2.23	531.15	80.49	533.19	5.31
LMNFO	528.77	12.17	1.16	531.41	73.94	533.20	13.88
LNFO	528.63	11.93	1.72	530.97	54.42	532.73	33.65

*quantified from XPS

^a S.A: BET surface area

* Quantified from XPS.

^a S.A: BET surface area.

corresponding to the oxygen ions shifts to lower binding energy from LMNFO catalyst to LSNFO catalyst. This result indicates that LSNFO catalyst has the highest lattice oxygen mobility compared to other tested catalysts and is in agreement with the TPD O₂ of LSNFO catalyst which also shows the highest lattice oxygen mobility.

The quantitative analysis of oxygen species is shown in Table 2. It can be seen that the amount of lattice oxygen per BET surface area on LSNFO catalyst is higher than LCNFO and LMNFO catalysts, confirming the highest lattice oxygen species on LSNFO catalyst. The similar result prepared using impregnation catalysts was reported in literature [57] that higher amount of lattice oxygen species is important for minimizing the carbon formation by forming oxy-carbonate species which can react with surface carbon to form CO.

3.5. Metal particle size of reduced catalysts

Fig. 5 shows the TEM figure of reduced catalysts. It can be seen that the metal size of LMNFO catalyst is similar to LSNFO catalyst, while the metal size of LCNFO catalyst is the biggest among other catalysts. Quantitatively, the metal size of LMNFO, LCNFO, and LSNFO catalyst is 7.4 nm, 12.9 nm, and 9.1 nm, respectively (See metal particle size distribution in Figure S3 in supplementary information). The smallest metal size of LMNFO catalyst is probably due to the stronger interaction between Ni–Fe and La–Mg to form solid solution as NiO and MgO was reported to be able to easily form solid solution, resulting in very fine particles [60–63]. The order of the metal size is in agreement with quantitative analysis of crystal size using XRD.

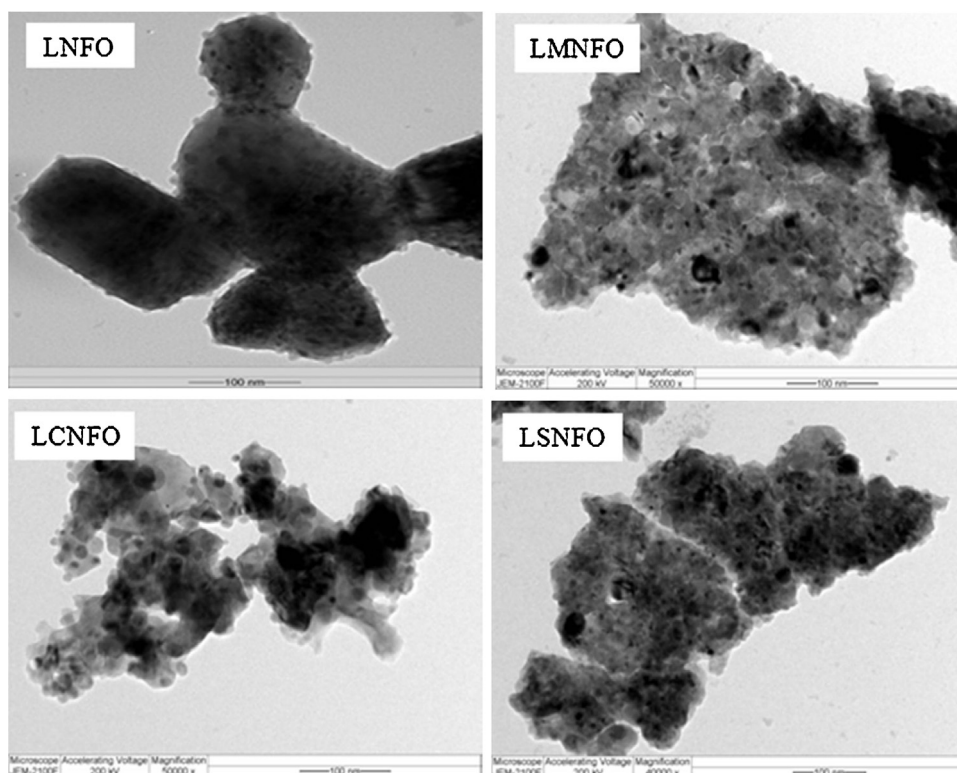


Fig. 5. TEM pictures of reduced catalysts.

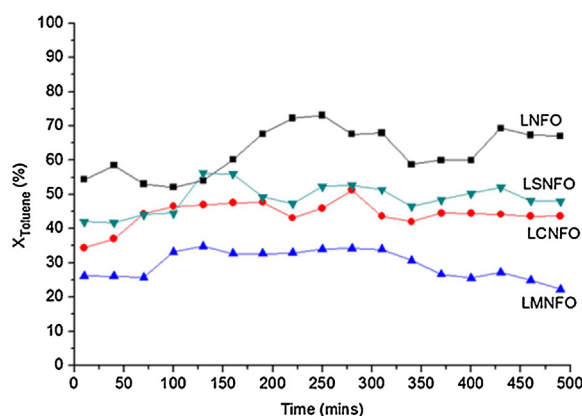


Fig. 6. Catalytic activity of $\text{La}_{0.8}\text{M}_{0.2}\text{Ni}_{0.8}\text{Fe}_{0.2}\text{O}_3$ catalyst at 650 °C. Reaction condition: toluene 188 $\mu\text{mol}/\text{min}$; steam 4444 $\mu\text{mol}/\text{min}$; He 5357 $\mu\text{mol}/\text{min}$; $W = 30$ mg; reaction temperature = 650 °C.

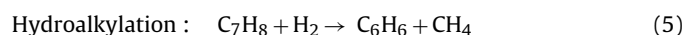
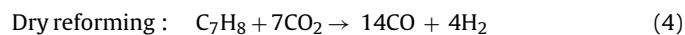
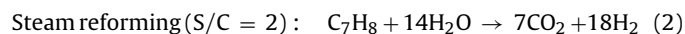
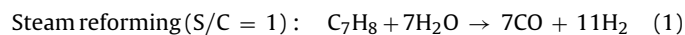
3.6. Catalytic performance for steam reforming of toluene

The reaction condition for catalytic test in this study is 650 °C with a steam to carbon ratio of 3.4, which follows the reaction condition used by Tomishige et al. [64]. They obtained 100% initial conversion of toluene at 650 °C using 100 mg Ni-Co/ Al_2O_3 catalyst. However, in order to clearly show the difference of catalytic activity among all catalysts, the amount of catalyst was reduced to 30 mg for each sample. Fig. 6 shows the catalytic activity of all perovskite catalysts for 8 h of reaction time. It can be seen that the order of catalytic activity decreases with the following order $\text{LSNFO} > \text{LCNFO} \gg \text{LMNFO}$. Table 3 shows the comparison between catalytic activity after 8 h of reaction time, amount of active sites, and amount of lattice oxygen. The higher amount of active sites is necessary for toluene decomposition. However, the order of catalytic activity does not follow the order of active sites measured by N_2O adsorption. Instead, it follows the order of lattice oxygen amount. The very low activity of LMNFO catalyst compared to LSNFO and LCNFO catalysts could also be due to the lower amount of active sites for reaction as shown by the lower N_2O adsorption of LMNFO catalyst and lower amount of lattice oxygen amount. This further shows that the amount of lattice oxygen has a significant effect on catalyst performance. The similar result was also observed on Ni/ $\text{La}_{0.7}\text{Sr}_{0.3}\text{O}_3$ catalyst for steam reforming of toluene [65] and alkaline earth metal-doped-Ni-catalyst for CO_2 reforming of methane [57].

Even though the activity of LSNFO catalyst is the highest among LCNFO and LMNFO catalysts, LNFO catalyst still has higher activity than LSNFO catalyst at reaction condition of 650 °C and S/C of 3.4. This result is surprising as alkaline earth metal addition to Ni catalyst has been reported to increase catalytic activity and stability in CO_2 reforming of methane [57] and steam reforming of toluene [65–67] due to the presence of lattice oxygen.

Basic metal addition such as K to Ni-catalyst was reported to promote formation of OH^- from water to enhance reaction [68]. This leads us to test the best two catalysts (LNFO and LSNFO catalysts) at severe condition such as low steam/carbon (S/C) ratio. The catalytic result shown in Fig. 7 reveals interesting phenomena. With the decreasing of S/C ratio, the order of catalytic result shows reverse trend. At S/C ratio of 2, LNFO catalyst has similar activity with LSNFO catalyst, but LSNFO catalyst outperforms LNFO catalyst at S/C ratio of 1. In detail, with decreasing steam/carbon ratio from 3.4 to 1, the catalyst activity of LNFO drops very fast from 67% to 20% in terms of toluene conversion while LSNFO catalyst shows a milder decrease in toluene conversion from 48% to 24%. However, the conversion of LSNFO catalyst at S/C ratio of 1 is higher than the conversion of LNFO catalyst. This change shows that LSNFO catalyst can perform well at low steam condition which is very beneficial since steam is expensive.

In order to understand this interesting phenomenon, the following reactions happening simultaneously in steam reforming of toluene needs to be considered [69,46]:



Reactions (1) and (2) represent the ideal steam reforming of toluene with S/C ratio of 1 and 2, respectively. Reaction (3) is water gas shift reaction which produces more H_2 . Basically, reaction (2) is a combination of reaction (1) and reaction (3). The produced CO_2 may react with toluene according to dry reforming of toluene (reaction (4)). Hydroalkylation (reaction (5)) also possibly occurs simultaneously to produce CH_4 . The CH_4 produced can then react

Table 3
Comparison catalytic activity after 8 h of reaction time, amount of active sites, and amount of lattice oxygen.

Catalyst	X toluene (%)	N_2O adsorption ($\mu\text{mol}/\text{g}$)	% area of lattice oxygen/BET S.A
LNFO	67.07	0.44	1.72
LMNFO	22.21	0.45	1.16
LCNFO	43.74	0.39	2.23
LSNFO	48.03	0.59	2.49

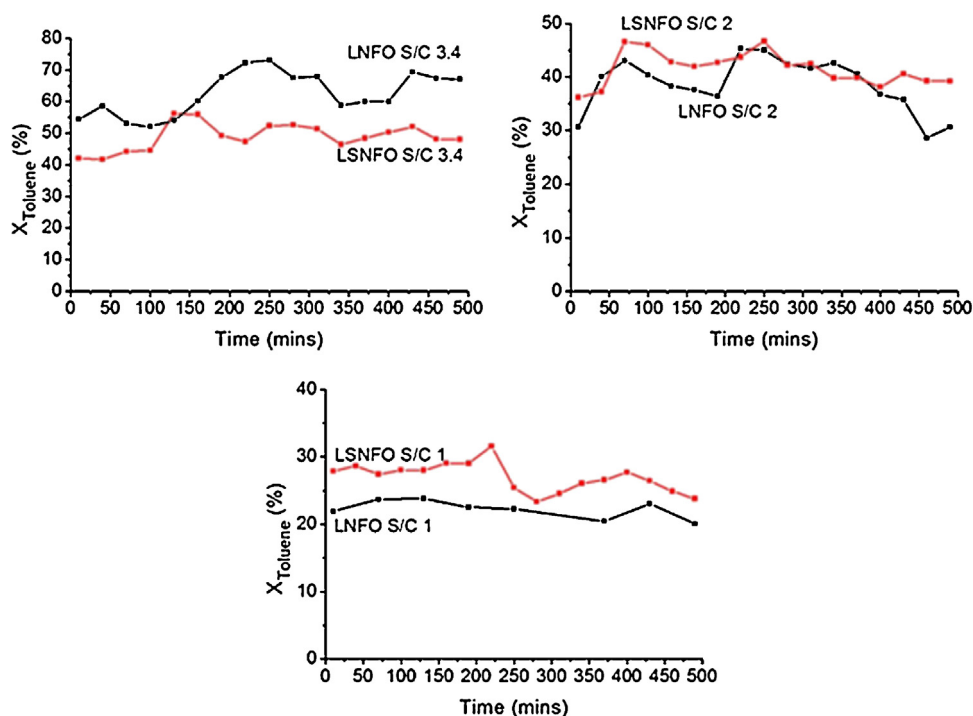


Fig. 7. Effect of steam/carbon ratio on LNFO and LSNFO catalysts at 650 °C.

Reaction condition: toluene 188 $\mu\text{mol/min}$; He 5357 $\mu\text{mol/min}$; $W = 30$ mg; reaction temperature = 650 °C.

with H_2O via steam reforming of methane (reaction (6)). However, reactions (4), (5), and (6) are less dominant compared to reactions (1) and (3).

Table 4 shows the detailed catalytic performance of LNFO and LSNFO catalysts at 650 °C and various S/C ratios after 8 h of reaction time. It can be seen that the H_2/CO ratio on LNFO and LSNFO catalysts decreases with decreasing S/C ratio due to less participation of water gas shift reaction to consume CO and produce more H_2 . Moreover, the amount of CO_2 on both catalysts is higher than the CO amount for S/C of 3.4 and 2, confirming the participation of water gas shift reaction. From the above possible reactions, the difference of catalytic performance of LNFO and LSNFO catalysts at various steam amount can be explained from water gas shift reaction since at low steam amount (S/C = 1), the participation of water gas shift reaction is much less dominant compared to reaction at high steam amount (S/C = 3). According to literature [70], the dissociation of water into adsorbed OH and H is a most important energy barrier in water gas shift reaction. Hence, the catalyst which can easily dissociate water into adsorbed OH and H will possibly have high activity in water gas shift reaction. Further characterization using TPD- H_2O and TPSR- H_2O on reduced catalysts is explained in the next section (Section 3.8).

Further study of reaction temperature effect was performed on LSNFO and LNFO catalysts at S/C of 1 and is shown in Fig. 8. It can be seen that with increasing reaction temperature, the activity of both

catalysts increases and the difference in activity between LNFO and LSNFO becomes more significant. The increase in conversion due to increasing temperature can compensate the decrease in conversion due to S/C reduction. It is also observed that the reactor blockage is observed for LNFO catalyst during reaction after 460 min of reaction time, showing very high carbon formation rate on LNFO catalyst. In contrast, the LSNFO catalyst can still maintain the activity above 70% toluene conversion for 8 h of reaction time due to the presence of lattice oxygen at 750 °C shown in TPD- O_2 result.

The stability test was then performed for LSNFO catalyst with 60 mg of catalyst amount. The result (Fig. 9) shows that LSNFO has good stability even though the steam used is very low (S/C = 1). Moreover, the toluene conversion is also very high, reaching more than 90% conversion along the reaction time.

3.7. Role of Sr in the presence of low steam amount

In order to understand the characteristic of LNFO and LSNFO catalysts in this reaction, TPD- H_2O was performed on reduced catalyst and the result is shown in Fig. 10. It can be seen that reduced LNFO catalyst shows one peak at 230–300 °C, attributing to the water desorption on La_2O_3 surface while reduced SNFO catalyst shows one peak at 400–470 °C, corresponding to water adsorption on SrO surface. On reduced LSNFO catalyst, two peaks are observed at 230–300 °C and 380–500 °C. The first peak corresponds to water

Table 4
Catalytic results of LNFO and LSNFO catalysts at 650 °C and various S/C ratio after 8 h of reaction time.

Catalysts	S/C	X_{toluene} (%)	Production rate ($\mu\text{mole/min}$)			Dry gas composition (%)			H_2/CO
			H_2	CO	CO_2	H_2	CO	CO_2	
LNFO	3.4	67.07	1331.47	421.00	459.81	60.19	19.03	20.78	3.16
	2	35.76	588.78	190.66	278.99	55.63	18.01	26.36	3.09
	1	20.05	360.72	133.28	129.96	57.81	21.36	20.83	2.71
LSNFO	3.4	48.03	934.82	242.55	388.16	59.71	15.49	24.79	3.85
	2	39.22	694.85	217.62	297.38	57.43	17.99	24.58	3.19
	1	24.96	413.48	173.76	154.06	55.78	23.44	20.78	2.38

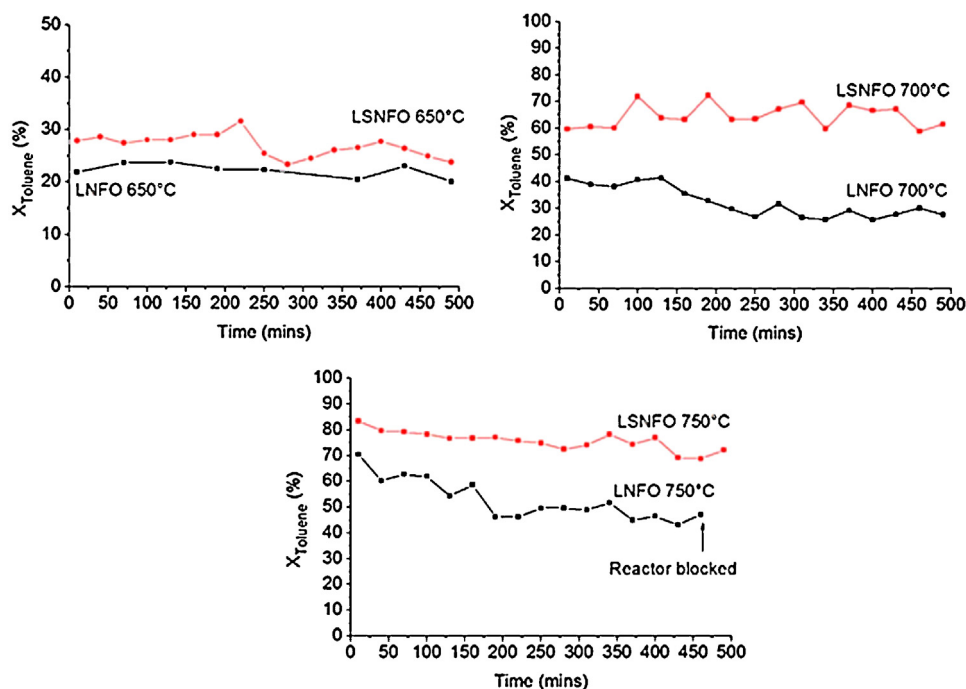


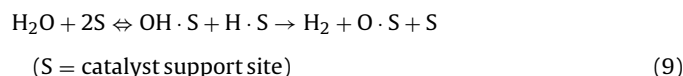
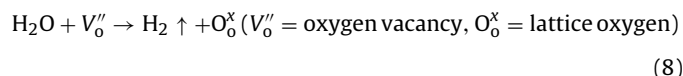
Fig. 8. Effect of temperature on LNFO and LSNFO catalysts at S/C = 1.

Reaction condition: toluene 188 $\mu\text{mol/min}$; steam 1316 $\mu\text{mol/min}$; He 5357 $\mu\text{mol/min}$; W = 30 mg.

desorption on La_2O_3 surface while the latter peak attributes to water desorption on SrO surface. The higher temperature of water desorption on SrO surface indicates that Sr has stronger binding with water than La. Moreover, it is interesting to observe that even though the amount of Sr is only 0.2, the area of water desorption peak on SrO surface is more than half of the one on La_2O_3 surface. Quantitatively, the total area of water desorption peak on LSNFO catalyst is almost 150% of the one on LNFO catalyst. This result shows that Sr can adsorb and desorb much more water than La.

Furthermore, the temperature-programmed surface reaction of water (TPSR- H_2O) was also performed on reduced catalysts. The difference between TPD- H_2O and TPSR- H_2O is that in TPSR- H_2O measurement, the water was introduced continuously using He as a carrier gas and H_2 production was monitored by mass spectrometer while in the TPD- H_2O measurement, water was only introduced at room temperature for 30 min followed by purging under He and the H_2O desorption was monitored by mass spectrometer. The TPSR- H_2O result in Fig. 11 shows that H_2 production was clearly observed

for LNFO and LSNFO catalysts at temperature of 590 °C. However, the intensity of H_2 produced from LNFO catalyst is higher than LSNFO catalyst. On the other hand, there is no H_2 produced from SNFO catalyst. The H_2 production from water can be expressed in the following reaction equations:



Based on the above equations, it can be explained that reaction (8) is not applicable for all catalysts since SNFO catalyst has no H_2 production. Reaction (9) is only applicable for LSNFO catalyst since only LSNFO catalyst has oxygen vacancy which can be seen

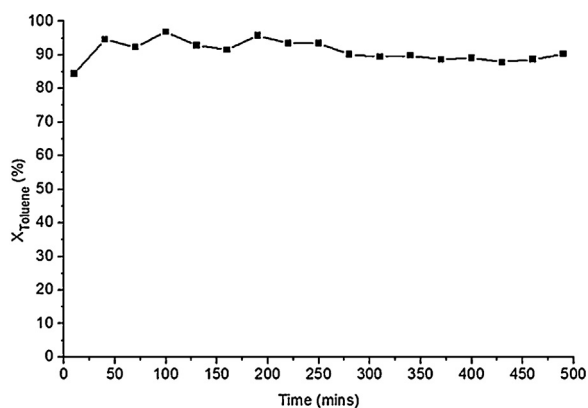


Fig. 9. Catalyst stability of LSNFO catalyst at 750 °C and S/C = 1.

Reaction condition: toluene 188 $\mu\text{mol/min}$; steam 1316 $\mu\text{mol/min}$; He 5357 $\mu\text{mol/min}$; W = 60 mg.

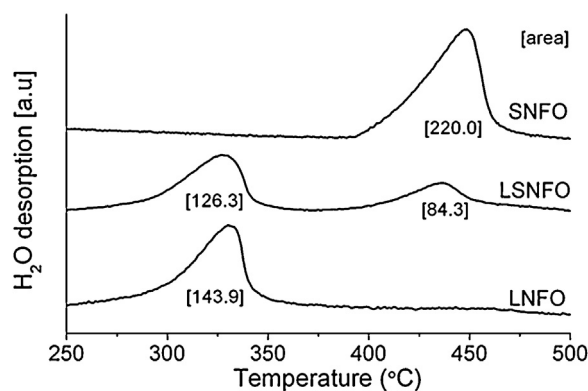


Fig. 10. TPD- H_2O profiles of reduced catalysts.

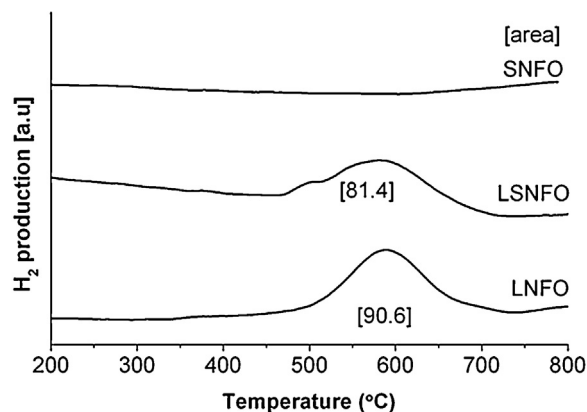


Fig. 11. TPSR-H₂O profiles of reduced catalysts.

from TPD-O₂ result (Fig. 3) while reaction 10 is applicable for only LNFO and LSNFO catalysts as both catalysts contain La₂O₃ which is known to be highly hygroscopic and can easily dissociate water into OH and H [71]. The higher H₂ production from LNFO catalyst is because LNFO catalyst contains 100% La₂O₃ while LSNFO catalyst only contains 80% La₂O₃. In addition, the hydrogen production due to oxygen vacancy on LSNFO catalyst should also be taken into account.

It is reported in literature [72] that toluene had competitive adsorption with water and could expel the weakly bound water on catalyst support. This means that in the low steam condition (S/C = 1), the water adsorbed on La₂O₃ of LNFO and LSNFO catalysts can be easily expelled by toluene while the water on SrO of LSNFO catalyst remains on the catalyst support. This strongly bound water on SrO is believed to spill-over to La₂O₃ for water dissociation into OH and H. Hence, LSNFO catalyst has better performance than LNFO catalyst at low steam condition. In contrast, in the high steam condition (S/C = 3.4), the excess of water during reaction can prevent

adsorption of toluene on the catalyst support, resulting in higher activity of LNFO catalyst compared to LSNFO catalyst.

By analyzing the catalytic performance, TPD-H₂O, and TPSR-H₂O results, it can be clearly seen that the roles of Sr are: (1) to create the oxygen vacancy so that the H₂ can be produced from water and the lattice oxygen can be replenished which later helps to remove the carbon and (2) to adsorb more water and desorb it at higher temperature. These roles are more pronounced at high temperature since lattice oxygen is only active at high temperature (around 750 °C as seen from TPD-H₂O of LSNFO catalyst).

3.8. Carbon formation on spent catalysts

During steam reforming of toluene reaction, the carbon deposition is likely to occur on catalyst surface and it can cause the catalyst deactivation. It is therefore important to characterize the spent catalyst using various methods to observe the type and amount of carbon deposition. Fig. 12 shows the FESEM images of spent catalyst after reaction at S/C of 3.4. It can be seen that all spent catalysts produce filamentous carbon even though the filamentous carbon on spent LSNFO catalyst looks like different among other spent catalysts.

The quantitative analysis of carbon deposition on spent catalyst was performed using TGA analysis and the results are shown in Fig. 13. It can be seen that the amount of carbon deposition on spent catalyst after reaction at 650 °C and S/C of 3.4 decreases with the order of LNFO > LMNFO > LCNFO > LSNFO. This order is exactly the same as the order of oxygen mobility shown via TPD-O₂ (Fig. 3) and XPS O 1s (Fig. 4 and Table 2) results which show the order of lattice oxygen of LSNFO > LCNFO > LMNFO > LNFO. With the decreasing of S/C ratio, the carbon deposition also decreased as shown in Fig. 13b due to the decrease in toluene conversion. With increasing temperature, the carbon deposition increases for LNFO catalyst due to increase in toluene conversion while for LSNFO catalyst, the carbon deposition decreases with increasing temperature since LSNFO

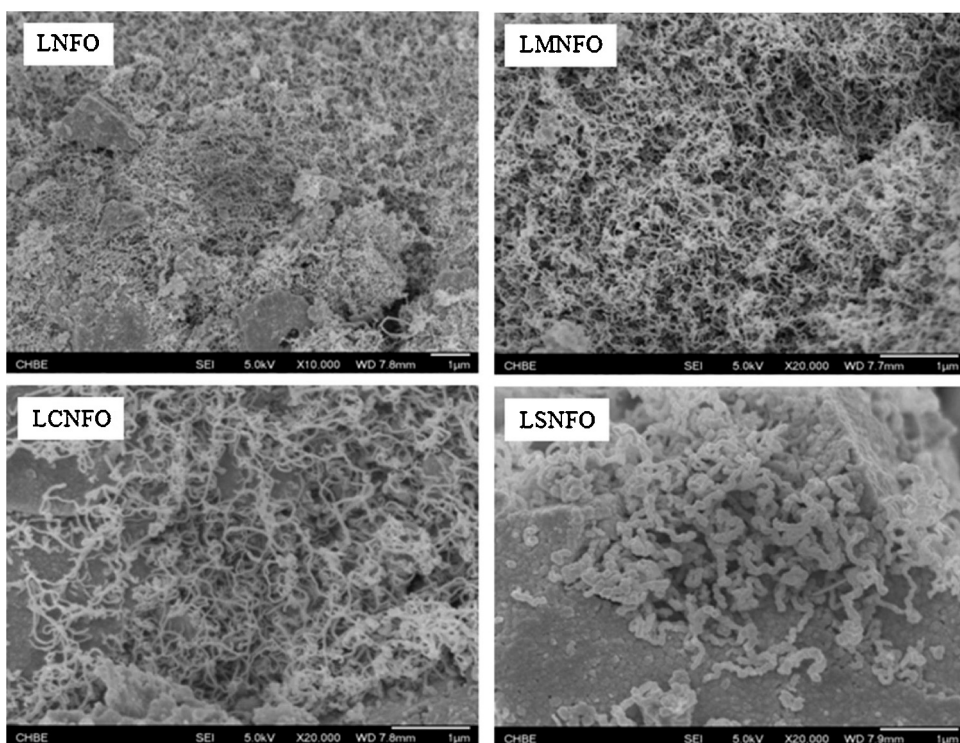


Fig. 12. FESEM images of spent catalysts.

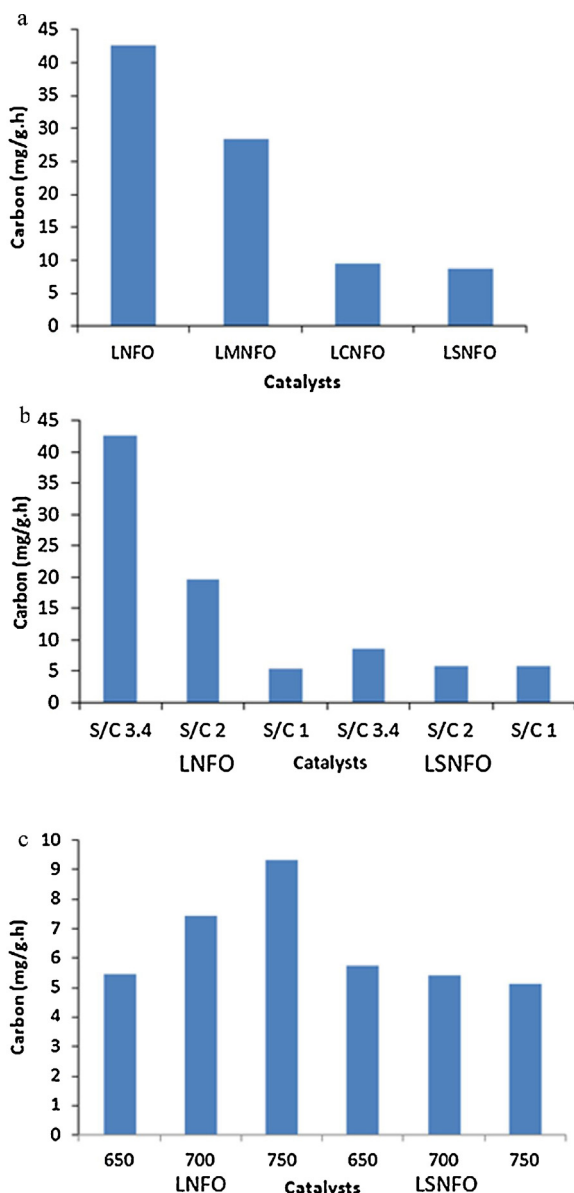


Fig. 13. Carbon formation rate of spent catalysts for (a) various alkaline earth metal addition; (b) various S/C ratio; and (c) various reaction temperature.

catalyst has lattice oxygen which can actively oxidize carbon deposition at the higher temperature.

4. Conclusion

The effect of alkali earth metal (Mg, Ca, and Sr) substitution to $\text{LaNi}_{0.8}\text{Fe}_{0.2}\text{O}_3$ (LNFO) perovskite catalyst was found to play an important role for steam reforming of toluene as a model compound of tar at high steam condition. The catalytic activity decreases with the order of $\text{La}_{0.8}\text{Sr}_{0.2}\text{Ni}_{0.8}\text{Fe}_{0.2}\text{O}_3$ (LSNFO) > $\text{La}_{0.8}\text{Ca}_{0.2}\text{Ni}_{0.8}\text{Fe}_{0.2}\text{O}_3$ (LCNFO) > $\text{La}_{0.8}\text{Mg}_{0.2}\text{Ni}_{0.8}\text{Fe}_{0.2}\text{O}_3$ (LMNFO) catalyst. The higher activity on LSNFO catalyst is due to higher amount of active sites and higher amount of lattice oxygen. The highest amount of lattice oxygen on LSNFO catalyst results in the lowest carbon formation among other studied catalysts.

LNFO catalyst has higher catalytic performance than LSNFO catalyst at high steam condition (S/C = 3.4). However, at low steam condition (S/C = 1), LSNFO catalyst shows superior catalytic performance than LNFO catalyst. Further characterization shows that Sr

of LSNFO catalyst can adsorb much more water and desorb water at higher temperature than LNFO catalyst. This strongly adsorbed water property of LSNFO catalyst enables this catalyst to have better catalytic performance at low steam condition.

Acknowledgements

The authors acknowledge financial support from National University of Singapore and NEA-ETRP (Project No. 1002 114, Research Grant No. 279-000-333-490). Usman Oemar sincerely thanks Dr. Yasotha Kathiraser, Dr. Jangam Ashok, Dr. Mo Liuye, and Mr. Saw Eng Toon for technical support and discussions.

Appendix A. Supplementary data

Supplementary data associated with this article can be found, in the online version, at <http://dx.doi.org/10.1016/j.apcatb.2013.10.001>.

References

- [1] H. de Lasa, E. Salaices, J. Mazumder, R. Lucky, Chem. Rev. 111 (2011) 5404–5433.
- [2] G.W. Huber, S. Iborra, A. Corma, Chem. Rev. 106 (2006) 4044–4098.
- [3] P.R. Buchiredy, R.M. Bricka, J. Rodriguez, W. Holmes, Energy Fuels 24 (2010) 2707–2715.
- [4] J. Han, H. Kim, Renew. Sust. Energy Rev. 12 (2008) 397–416.
- [5] A.V. Bridgwater, Appl. Catal. A 116 (1994) 5–47.
- [6] R. Coll, J. Salvadó, X. Farriol, D. Montané, Fuel Process. Technol. 74 (2001) 19–31.
- [7] C. Wu, P.T. Williams, Biofuels 2 (2011) 451–464.
- [8] T. Kimura, T. Miyazawa, J. Nishikawa, S. Kado, K. Okumura, T. Miyao, S. Naito, K. Kunimori, K. Tomishige, Appl. Catal. B 68 (2006) 160–170.
- [9] J. Nishikawa, T. Miyazawa, K. Nakamura, M. Asadullah, K. Kunimori, K. Tomishige, Catal. Commun. 9 (2008) 195–201.
- [10] G. Guana, G. Chena, Y. Kasai, E.W.C. Lim, X. Hao, M. Kaewpanha, A. Abuliti, C. Fushimi, A. Tsutsumi, Appl. Catal. B 115–116 (2012) 159–168.
- [11] U. Oemar, K. Hidayat, S. Kawi, Int. J. Hydrogen Energy 38 (2013) 5525–5534.
- [12] L. Wang, D. Li, M. Koike, S. Koso, Y. Nakagawa, Y. Xu, K. Tomishige, Appl. Catal. A 392 (2011) 248–255.
- [13] M. Koike, D. Li, Y. Nakagawa, K. Tomishige, ChemSusChem 5 (2012) 2312–2314.
- [14] B. Zhang, X. Tang, Y. Li, Y. Xu, W. Shen, Int. J. Hydrogen Energy 32 (2007) 2367–2373.
- [15] X. Hu, G. Lu, J. Mol. Catal. A 261 (2007) 43.
- [16] N. Iwasa, T. Yamane, M. Takei, J. Ozaki, M. Arai, Int. J. Hydrogen Energy 35 (2010) 110–117.
- [17] L. Wang, Y. Hisada, M. Koike, D. Li, H. Watanabe, Y. Nakagawa, K. Tomishige, Appl. Catal. B 121–122 (2012) 95–104.
- [18] M. Koike, Y. Hisada, L. Wang, D. Li, H. Watanabe, Y. Nakagawa, K. Tomishige, Appl. Catal. B 140–141 (2013) 652–662.
- [19] D. Świerczyński, S. Libs, C. Courson, A. Kiennemann, Appl. Catal. B 74 (2007) 211–222.
- [20] K. Nakamura, T. Miyazawa, T. Sakurai, T. Miyao, S. Naito, N. Begum, K. Kunimori, K. Tomishige, Appl. Catal. B 86 (2009) 36–44.
- [21] D. Li, L. Wang, M. Koike, Y. Nakagawa, K. Tomishige, Appl. Catal. B 102 (2011) 528–538.
- [22] F. Bimbela, D. Chen, J. Ruiz, L. Garcia, J. Arauzo, Appl. Catal. B 119–120 (2012) 1–12.
- [23] I. Zamboni, C. Courson, D. Niznansky, A. Kiennemann, Appl. Catal. B (2013), <http://dx.doi.org/10.1016/j.apcatb.2013.02.046>.
- [24] H. Jeong, K.I. Kim, D. Kim, I.K. Song, J. Mol. Catal. A 246 (2006) 43–48.
- [25] T. Horiuchi, K. Sakuma, T. Fukui, Y. Kubo, T. Osaki, T. Mori, Appl. Catal. A 144 (1996) 111–120.
- [26] Y.H. Hu, E. Ruckenstein, Chem. Rev. 44 (2002) 423–453.
- [27] H. Inokawa, S. Nishimoto, Y. Kameshima, M. Miyake, Int. J. Hydrogen Energy 36 (2011) 15195–15202.
- [28] C.K.S. Choong, Z. Zhong, L. Huang, Z. Wang, T.P. Ang, A. Borgna, J. Lin, L. Hong, L. Chen, Appl. Catal. A 407 (2011) 145–154.
- [29] C.K.S. Choong, L. Huang, Z. Zhong, J. Lin, L. Hong, L. Chen, Appl. Catal. A 407 (2011) 155–162.
- [30] T. Viinikainen, H. Rönkkönen, H. Bradshaw, H. Stephenson, S. Airaksinen, M. Reinikainen, P. Simell, O. Krause, Appl. Catal. A 362 (2009) 169–177.
- [31] T. Mendiara, J.M. Johansen, R. Utrilla, P. Geraldo, A.D. Jensen, P. Glarborg, Fuel 90 (2011) 1049–1060.
- [32] L. Devi, K.J. Ptasiński, F.J.J.G. Janssen, Biomass Bioenergy 24 (2003) 125–140.
- [33] C. Li, D. Hirabayashi, K. Suzuki, Appl. Catal. B 88 (2009) 351–360.
- [34] M. Koike, C. Ishikawa, D. Li, L. Wang, Y. Nakagawa, K. Tomishige, Fuel 103 (2013) 122–129.
- [35] J. Nishikawa, K. Nakamura, M. Asadullah, T. Miyazawa, K. Kunimori, K. Tomishige, Catal. Today 131 (2008) 146–155.
- [36] Y. Lu, S. Li, L. Gu, X. Zhang, Int. J. Hydrogen Energy 35 (2010) 7161–7168.

- [37] R. Zhang, Y. Wang, R.C. Brown, *Energy Convers. Manage.* 48 (2007) 68–77.
- [38] A. Bampennrat, V. Meeyoo, B. Kitiyanan, P. Rangsunvigit, T. Rirksomboon, *Appl. Catal. A* 373 (2010) 154–159.
- [39] K. Soongprasit, D. Aht-Ong, V. Sricharoenchaiikul, D. Atong, *Curr. Appl. Phys.* 12 (2012) S80–S88.
- [40] M.A. Peña, J.L.G. Fierro, *Chem. Rev.* 101 (2001) 1981–2017.
- [41] S. Tada, M. Yokoyama, R. Kikuchi, T. Haneda, H. Kameyama, *J. Phys. Chem. C* 117 (2013) 14652–14658.
- [42] K. Sutthiumporn, T. Maneerung, Y. Kathiraser, S. Kawi, *Int. J. Hydrogen Energy* 37 (2012) 11195–11207.
- [43] T. Maneerung, K. Hidajat, S. Kawi, *Catal. Today* 171 (2011) 24–35.
- [44] H. Provendier, C. Petit, A. Kiennemann, *C. R. Acad. Sci. IIC* 4 (2001) 57–66.
- [45] H. Provendier, C. Petit, C. Estournès, S. Libs, A. Kiennemann, *Appl. Catal. A* 180 (1999) 163–173.
- [46] S. Rapagná, H. Provendier, C. Petit, A. Kiennemann, P.U. Foscolo, *Biomass Bioenergy* 22 (2002) 377–388.
- [47] S.M. de Lima, J.M. Assaf, *Catal. Lett.* 108 (2006) 63–70.
- [48] K. Chen, Y. Fan, Z. Hu, Q. Yan, *J. Solid State Chem.* 121 (1996) 240–246.
- [49] H. Provendier, C. Petit, C. Estournès, A. Kiennemann, *Stud. Surf. Sci. Catal.* 119 (1998) 741–746.
- [50] E. Ruckenstein, Y.H. Hu, *Appl. Catal. A* 133 (1995) 149–161.
- [51] E. Ruckenstein, Y.H. Hu, *Appl. Catal. A* 183 (1999) 85–92.
- [52] U. Oemar, K. Hidajat, S. Kawi, *Appl. Catal. A* 402 (2011) 176–187.
- [53] S. Kaliaguine, A. Van Neste, V. Szabo, J.E. Gallot, M. Bassir, R. Muzychuk, *Appl. Catal. A* 209 (2001) 345–358.
- [54] D. Ferri, L. Forni, *Appl. Catal. B* 16 (1998) 119–126.
- [55] S. Royer, A. Van Neste, R. Davidson, S. McIntyre, S. Kaliaguine, *Ind. Eng. Chem. Res.* 43 (2004) 5670–5680.
- [56] T. Seiyama, N. Yamazoe, K. Eguchi, *Ind. Eng. Chem. Prod. Res. Dev.* 24 (1985) 19–27.
- [57] K. Sutthiumporn, S. Kawi, *Int. J. Hydrogen Energy* 36 (2011) 14435–14446.
- [58] A.F. Carley, M.W. Roberts, A.K. Santra, *J. Phys. Chem. B* 101 (1997) 9978–9983.
- [59] G.U. Kulkarni, C.N.R. Rao, M.W. Roberts, *J. Phys. Chem.* 99 (1995) 3310–3316.
- [60] M. Nurunnabi, Y. Mukainakano, S. Kado, B. Li, K. Kunimori, K. Suzuki, K. Fujimoto, K. Tomishige, *Appl. Catal. A* 299 (2006) 145–156.
- [61] M. Nurunnabi, B. Li, K. Kunimori, K. Suzuki, K. Fujimoto, K. Tomishige, *Appl. Catal. A* 292 (2005) 272–280.
- [62] Y. Chen, O. Yamazaki, K. Tomishige, K. Fujimoto, *Catal. Lett.* 39 (1996) 91–95.
- [63] Y.H. Hu, E. Ruckenstein, *Catal. Rev.* 44 (2002) 423–453.
- [64] L. Wang, D. Li, M. Koike, H. Watanabe, Y. Xu, Y. Nakagawa, K. Tomishige, *Fuel* 112 (2013) 654–661.
- [65] D. Mukai, S. Tochiya, Y. Murai, M. Imori, T. Hashimoto, Y. Sugiura, Y. Sekine, *Appl. Catal. A* 453 (2013) 60–70.
- [66] Y. Sekine, D. Mukai, Y. Murai, S. Tochiya, Y. Izutsu, K. Sekiguchi, N. Hosomura, H. Arai, E. Kikuchi, Y. Sugiura, *Appl. Catal. A* 451 (2013) 160–167.
- [67] K. Murata, L. Wang, M. Saito, M. Inaba, I. Takahara, N. Mimura, *Energy Fuels* 18 (2004) 122–126.
- [68] M.C. Demicheli, D. Duprez, J. Barbier, O.A. Ferretti, E.N. Ponzi, *J. Catal.* 145 (1994) 437–449.
- [69] L.D. Felice, C. Courson, P.U. Foscolo, A. Kiennemann, *Int. J. Hydrogen Energy* 36 (2011) 5296–5310.
- [70] C. Ratnasamy, J.P. Wagner, *Catal. Rev.* 51 (2009) 325–440.
- [71] J. Kwon, M. Dai, M.D. Halls, E. Langereis, Y.J. Chabal, R.G. Gordon, *J. Phys. Chem. C* 113 (2009) 654–660.
- [72] A.W. Heinen, J.A. Peters, H.V. Bakkum, *Appl. Catal. A* 194–195 (2000) 193–202.